OPTICA QUANTUM

Loss-resilient, x ray interaction-free measurements

RON COHEN,[1] SHARON SHWARTZ,[2] AND ELIAHU COHEN[1,*] [ID]

[1]*Faculty of Engineering and Institute of Nanotechnology and Advanced Materials, Bar-Ilan University, Ramat Gan 5290002, Israel*
[2]*Department of Physics and Institute of Nanotechnology and Advanced Materials, Bar-Ilan University, Ramat Gan 5290002, Israel*
*eliahu.cohen@biu.ac.il

Interaction-free measurement (IFM) is a promising technique for low-dose detection and imaging, offering the unique advantage of probing an object with an overall reduced absorption of the interrogating photons. We propose an experiment to demonstrate IFM in the single x ray photon regime. The proposed scheme relies on the triple-Laue (LLL) symmetric x ray interferometer, where each Laue diffraction acts as a lossy beam splitter. In contrast to many quantum effects which are highly vulnerable to loss, we show that an experimental demonstration of this effect in the x ray regime is feasible and can achieve detection with reduced dose and high IFM efficiency even in the presence of substantial loss in the system. The latter aspect is claimed to be a general property of IFM based on our theoretical analysis. We scrutinize two suitable detection schemes that offer a dose reduction of up to half compared with direct detection. The successful demonstration of IFM with x rays promises intriguing possibilities for measurements with reduced dose, mainly advantageous for biological samples, where radiation damage is a significant limitation.

1. INTRODUCTION

In quantum mechanics, the collapse or reduction of the wave function due to measurement may occur even in cases of "non-detection" events, where there appears to be no interaction between the measurement device and the system. The origin of this idea is rooted in Renninger's "negative-result" experiment [1]. The notion of an "interaction-free" quantum measurement, first coined by Dicke [2], describe a scenario in which a non-scattering event of a photon alters the wave function of an atom, although the quantum state of the electromagnetic field has not been affected. Later works introduced interaction-free measurement (IFM) [3–5] in a somewhat different and more applicable context, for which detection of an object is possible, without absorption or scattering of the probing particle by the object. This uniquely quantum effect, known also as the Elitzur–Vaidman bomb tester (see Fig. 1), relies on the distinction between a scenario in which a particle interferes with itself and when it takes a certain path and thus does not interfere. Therefore, the presence of an object which obstructs the interference can be inferred by the detectors and thus an object can be detected without interacting with the particle. Since the process is statistical, it is useful to define a figure of merit for the efficiency of IFM, which is the ratio of interaction-free detection events and the total number of detection events. Initial experimental demonstrations of this effect [5] achieved IFM efficiencies of $\eta < \frac{1}{2}$ and later demonstrations [6,7] achieved high IFM efficiencies $(\eta > \frac{1}{2})$, by utilizing the quantum Zeno effect (i.e., repeated interrogation [5]). These demonstrations inspired the development of IFM-based low-dose imaging techniques [8–10]. Given the delicate nature of biological samples, the utilization of IFM, particularly x ray IFM, presents a compelling opportunity, as envisaged in Refs. [11,12].

There are several advantages to employing IFM with x rays for biomedical imaging. The non-invasive capabilities of x rays make them a unique tool for imaging of internal biological structures, including bones and organs. Furthermore, commercially available x ray detectors can reach nearly 100% efficiency with low dark current and photon number resolving capabilities over a very broad spectral range [13,14]. The primary method for generating single x ray photons is through heralding using spontaneous parametric downconversion (SPDC) [15,16]. Radioactive sources of Mössbauer nuclei with a cascade scheme provide another method for generating and controlling single γ-ray photons [17]. In addition, quantum recoil was recently suggested as a promising method for generating tunable single x ray photons [18]. Furthermore, an attenuated x ray coherent source can also be used to generate single photons by post-selection. Also, there is a wide variety of x ray interferometers available [19–22]. For the purpose of x ray IFM, we note the triple-Laue (LLL) [23] and Fabry–Pérot (FP) interferometers [21,22]. The former can be used for a proof-of-concept demonstration as discussed below, and the latter can be employed for implementing high-efficiency IFM [7,24]. We emphasize that at first glance, there appears to be a potentially significant challenge for the implementation of x ray IFM. Absorption has proven to be significant in almost all previously reported x ray interferometers, typically reducing the efficiency of quantum effects. However, we show that IFM exhibits notable resilience to losses, unlike many other quantum effects and technologies. Therefore, the utilization of x ray IFM holds particular promise
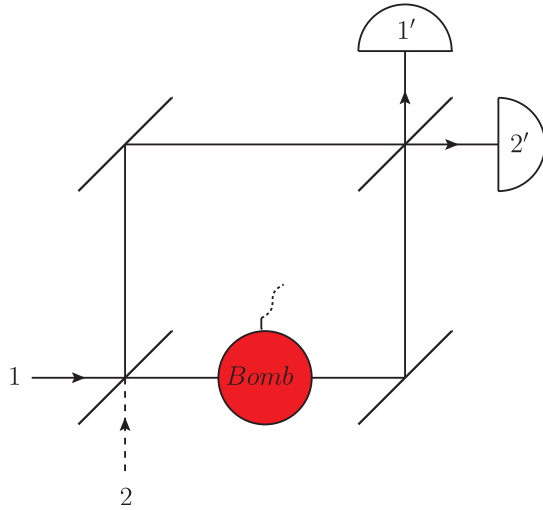
Fig. 1. The Elitzur–Vaidman bomb tester scheme: a live bomb or a dud is inserted into a symmetric lossless Mach–Zehnder interferometer (the dashed line indicates a vacuum input). In the absence of a live bomb, a photon will be detected at port #2′ with certainty, while port #1′ will never register a photon. In the presence of a live bomb, a photon may be registered in port #1′, hence enabling interaction-free detection.

in this regard. A first experimental demonstration of x ray IFM can pave the way for the development of low-dose bio-imaging schemes.

Here we analyze the feasibility of demonstrating this effect in a lossy LLL system, in the single x ray photon regime. We theoretically modeled the LLL system as being comprised of four identical lossy beam splitters, such that each Laue diffraction acts as a beam splitter. We identified two possible detection schemes, characterized their efficiencies and capabilities for reduced-dose detection, and concluded that an x ray IFM demonstration is feasible even in the lossy regime.

2. PROPOSED EXPERIMENTAL SCHEME

Our proposal is based on the LLL interferometer [23], which operates similarly to the Mach–Zehnder interferometer but specifically designed for x rays. The LLL interferometer is constructed by cutting two wide grooves in a single crystal block to form three plates, as depicted in Fig. 2(a). The first plate operates as a beam splitter, the second plate operates as two mirrors, and the third plate is another beam splitter. In each plate a Laue diffraction occurs, such that different portions of the beam are transmitted, diffracted, and absorbed. The ratio between the transmission and diffraction is determined by the width of the plates, incident angle, and the spectral profile of the beam. Therefore, control of the ratio of transmission and reflection is possible, by tuning the incident angle with respect to Bragg's angle. Controlling this ratio is crucial for optimizing IFM efficiency, a point that will be further elucidated in the next section. The same system can be theoretically described as a Mach–Zehnder interferometer, in which each mirror is replaced by a beam splitter, as depicted in Fig. 2(b). The system consists of four identical beam splitters (BS_1, BS_2, M_1, M_2), with identical transmission ($\tilde{T}$), reflection ($\tilde{R}$), and loss (τ) coefficients. We define the lossless transmission and reflection coefficients
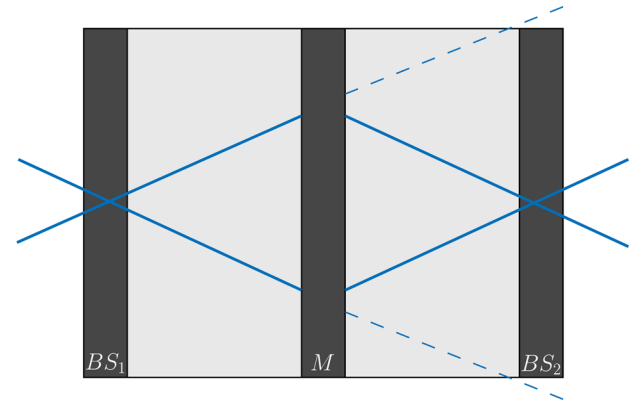
(a) Triple-Laue symmetric interferometer
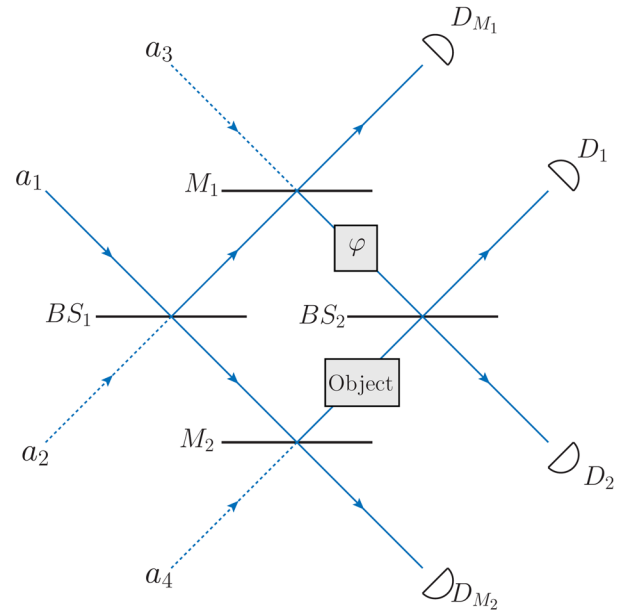
(b) Theoretical representation of the LLL system

Fig. 2. (a) The LLL system: the first plate (BS_1) acts as the first beam splitter. The second plate (M) acts as two mirrors. The third plate (BS_2) acts as the second beam splitter. (b) Theoretical representation of the LLL system: input operators undergo first beam splitter (BS_1). Each beam is then reflected by the two mirrors (M_1, M_2) and each such mirror can be considered to be a beam splitter. The reflected beam from the first mirror undergoes a phase shift φ, and finally passes through the second beam splitter (BS_2). Thereafter, the reflected beam from the second mirror is completely absorbed by an object. The dashed lines indicate vacuum input.

as (T, R), respectively, such that

$$\begin{aligned} \tilde{R} &= \tau R, \qquad \tilde{T} = \tau T, \\ R + T &= 1, \quad \tilde{R} + \tilde{T} = \tau, \end{aligned} \tag{1}$$

where the parameter τ determines the loss, such that it is lossless for $\tau = 1$ and otherwise $0 \leq \tau < 1$. In addition, we consider a possible phase term ($P(\varphi)$) and the possibility of an object lying on one of the arms.

We utilize the Heisenberg picture, in which we evolve in time the input operators. In our scheme, we consider four input operators. The two input operators for BS_1 are a_1 and a_2, and the operators for the vacuum inputs of the mirrors are a_3 (M_1)

and a_4 (M_2). Except for the phase term $P(\varphi)$, all other optical components are lossy and therefore, introduce noise. Consequently, noise operators are included in the transformation of each lossy component, and their magnitude is proportional to the loss. Theoretically, each optical component is described by a linear transformation acting on an input operator vector $\boldsymbol{a}_{in}$:

$$
\boldsymbol{a}_{in} = \begin{pmatrix} \boldsymbol{a} \\ \boldsymbol{a}_n \end{pmatrix},
$$

$$
\boldsymbol{a} = \begin{pmatrix} a_3 \\ a_1 \\ a_2 \\ a_4 \end{pmatrix}, \quad \boldsymbol{a}_n = \begin{pmatrix} a_{n1} \\ a_{n2} \\ \vdots \\ a_{n8} \end{pmatrix}. \tag{2}
$$

The input operator vector $\boldsymbol{a}_{in}$ includes our physical input and noise operators denoted as $\boldsymbol{a}, \boldsymbol{a}_n$, respectively.

Schematically, each optical component (OC) can therefore be expressed as

$$
\text{OC} = \begin{pmatrix} \sqrt{\tau} U_{OC} & \sqrt{1-\tau} n_{OC} \\ \mathbb{0} & \mathbb{1} \end{pmatrix}, \tag{3}
$$

where U_{OC} represents an optical component acting on the input modes (a_1, a_2, a_3, a_4) weighted by the square root of the loss parameter, and to introduce vacuum noise (for $\tau < 1$), we employ n_{OC} to distribute noise operators for the relevant modes [for more details, see Eqs. (S14)–(S16) in Supplement 1]. Clearly, the added noise is proportional to the loss, e.g., for the lossless case ($\tau = 1$) the added noise vanishes.

For this system, there are five possible transformations, one for each beam splitter/mirror and for the phase term ($BS_1, BS_2, M_1, M_2, P(\varphi)$); their explicit form is stated in the first part of Supplement 1. Realistic representation of the optical components presented here, can be effectively realized by modeling Laue diffraction as a lossy beam splitter transformation as shown in Section 4.

IFM detection relies on statistical contrast in output port measurements between scenarios in which an object is present and absent. The best possible contrast is achieved when we have an ideal dark port (in the absence of an object), namely, a port for which the detector will never measure a photon due to complete destructive interference. In this case, a photon can be detected at our designated dark port only if an object obstructs the interference. Since the object creates path distinguishability for the photon, object detection can be achieved without it absorbing any radiation. To quantify the efficiency of our detection, we use the conventional IFM efficiency [5] figure of merit

$$
\eta = \frac{P(\text{det})}{P(\text{det}) + P(\text{abs})}, \tag{4}
$$

where $P(\text{det})$ is the probability of detecting an object without absorption by the object and $P(\text{abs})$ is the probability for the object to absorb the photon. This figure of merit was originally conceived for an ideal (lossless) system, for which it quantifies the portion of detection events that are interaction-free (since absorption indicates the presence of an object). However, it still bears meaning in the general (lossy) case, since we are only concerned with absorption events by the object which increase the radiation dose.

Employing IFM can lead to detection with reduced dosage to the object, provided absorption events can be used to extract information on the presence of the object or that the IFM efficiency exceeds $\frac{1}{2}$. In the ideal lossless case (see Fig. 1), a loss of a photon can only be due to absorption by the object, and therefore, provides a detection channel with 100% certainty.

Dose reduction would require comparing the dosage in the object for a fixed number of detections with the case of direct illumination. In the case of direct illumination with single x ray photons and perfect detector behind the completely absorbing object, for each detection event (no click on the detector) there is one unit of dosage. To quantify dose reduction, we define

$$
\eta^{\text{dose}} = \frac{\overline{\#\text{detection events}} - \overline{\#\text{absorption events by the object}}}{\overline{\#\text{detection events}}}. \tag{5}
$$

This quantity represents the percentage of dose reduction achieved in the detection. For example, when $\eta^{\text{dose}} = 1$ means that a detection was made without any radiation to the object. In direct illumination, every detection event is also an absorption event, and therefore $\eta^{\text{dose}}_{\text{direct det.}} = 0$. This means that the threshold for dose reduction is $\eta^{\text{dose}} > 0$, for which there are more detection events than absorption events and thus a reduction of dosage is achieved.

In an ideal (lossless) IFM scheme, there are two detection channels, one is by IFM detection and the other by absorption by the object. Considering only these detection channels (while disregarding any other event), the probability for IFM detection is given by η (see Eq. (4)) and the probability of detection by absorption (by the object) is given by its complement $\eta' = \frac{P(\text{abs})}{P(\text{det}) + P(\text{abs})}$. Given these, we find that for an ideal (lossless) IFM scheme

$$
\eta^{\text{dose}} = \frac{(\eta + \eta') - \eta'}{\eta + \eta'} = \eta. \tag{6}
$$

This means that in the lossless case, the definition of η^{dose} coincides with the definition of the IFM efficiency (Eq. (4)). However, this will not be true in a lossy system. For a lossy interferometer, a loss event will not indicate with 100% certainty the presence of an object. Instead, when a photon is lost, it will be due to absorption by the object or the interferometer. Despite this ambiguity, it is still possible to distinguish between the two scenarios. For the purpose of detection by absorption, we only need consider events which may be distinguished statistically by the presence or absence of an object while disregarding IFM detection events. The remaining events are the loss of a photon and a detection of a photon by the other remaining port (we shall refer to it as the bright port) denoted in Fig. 1 as #2′. In the ideal (lossless) IFM scheme, readings in the bright port would not yield any information regarding the presence of an object, since such readings are possible in both cases. However, these readings become important when the interferometer is lossy, since the relation between the probability of losing a photon (P_l) and detecting a photon in the bright port (P_b) depend on the presence or absence of an object. This difference allows in principle for us to detect an object in absorption events. We therefore define the following distinguishability estimator:

$$
C(n_l, n_b)
$$

$$
= \frac{P(n_l, n_b | \text{object}) P(\text{object})}{P(n_l, n_b | \text{object}) P(\text{object}) + P(n_l, n_b | \text{no object}) P(\text{no object})}, \tag{7}
$$

where (n_l, n_b) are the number of events for losing a photon and measuring a photon in the bright port, respectively; ($P(n_l, n_b | \text{object}), P(n_l, n_b | \text{no object})$) are the conditional probabilities for the distribution of events (n_l, n_b), given the presence or

absence of an object, respectively; and $(P(\text{object}), P(\text{no object}))$ are the prior probabilities for the presence and absence of an object, respectively. With no prior knowledge, we can assume that $P(\text{object}) = P(\text{no object}) = \frac{1}{2}$. These binomial probabilities are given by

$$P(n_l, n_b | s) = \binom{n_l + n_b}{n_l} \tilde{P}_l^{n_l}(s) \tilde{P}_b^{n_b}(s),$$

$$\tilde{P}_l(s) = \frac{P_l(s)}{P_l(s) + P_b(s)}, \quad \tilde{P}_b(s) = \frac{P_b(s)}{P_l(s) + P_b(s)}, \tag{8}$$

where $s \in \{\text{object}, \text{no object}\}$ and $P_l(s) = 1 - \sum_{j \in \text{All ports}} P_j(s)$.

In a real experiment, the confidence $C(n_l, n_b)$ can be calculated and updated with each additional experimental run (while a photon has yet to reach the dark port) and can be used to estimate the presence or absence of an object. It represents the degree of confidence an object is present, deduced from the statistical data the experimentalist accumulated. For the purpose of a theoretical analysis, the expected confidence $C \equiv \overline{C(n_l, n_b)}_{\text{object}}$ can be regarded as the probability of success in detecting an object via absorption events. It can be calculated using the average values of (n_l, n_b) for a single absorption event by the object, such that $n_l = \frac{P_l(\text{object})}{P(\text{abs})}, n_b = \frac{P_b(\text{object})}{P(\text{abs})}$. Therefore, the dose reduction is given by

$$\eta^{\text{dose}} = \frac{(\eta + C\eta') - \eta'}{\eta + C\eta'} = \frac{P(\text{det}) - (1 - C)P(\text{abs})}{P(\text{det}) + CP(\text{abs})}. \tag{9}$$

The confidence level required for dose reduction is $C > 1 - \frac{P(\text{det})}{P(\text{abs})}$.

3. DETECTION CONFIGURATIONS

Generally, depending on the type of interferometer used, there can be several configurations for which a dark port is achieved, and for each configuration there is a different detection efficiency.

For single photons entering the interferometer (Fig. 2) in the absence of an object, the mean photon number at the output ports is shown in Table 1. In the presence of an object, the mean photon number at the output ports is shown in Table 2 and the variance in photon number in these tables is $(\Delta^2 N_k) = \langle N_k \rangle (1 - \langle N_k \rangle)$.

Note that due to the symmetry of the LLL system, these results are valid for a general beam splitter, and do not depend on the relative phase between the output modes of the beam splitter (provided they are identical).

We consider two configurations in which a dark port is achievable and, correspondingly, two detection configurations which depend on the transmission ($\tilde{T}$), reflection ($\tilde{R}$), and the phase φ of the interferometer. In the first configuration we consider, the

Table 1. Mean Photon Number at the Output Ports for Input States $a_1^\dagger|0\rangle = |1\rangle_{1a}$ and $a_2^\dagger|0\rangle = |1\rangle_{2a}$ in the Absence of an Object

Ports \ Measurements	Input State $a_1^\dagger\|0\rangle = \|1\rangle_{1a}$	Input State $a_2^\dagger\|0\rangle = \|1\rangle_{2a}$
Port #3 $(D_{M_1}) \backslash \langle N_3 \rangle$	$\tilde{R}\tilde{T}$	$\tilde{T}^2$
Port #1 $(D_1) \backslash \langle N_1 \rangle$	$\tilde{R}^3 - 2\tilde{R}^2\tilde{T}\cos(\varphi) + \tilde{R}\tilde{T}^2$	$4\tilde{R}^2\tilde{T}\cos^2\left(\frac{\varphi}{2}\right)$
Port #2 $(D_2) \backslash \langle N_2 \rangle$	$4\tilde{R}^2\tilde{T}\cos^2\left(\frac{\varphi}{2}\right)$	$\tilde{R}^3 - 2\tilde{R}^2\tilde{T}\cos(\varphi) + \tilde{R}\tilde{T}^2$
Port #4 $(D_{M_2}) \backslash \langle N_4 \rangle$	$\tilde{T}^2$	$\tilde{R}\tilde{T}$

Table 2. Mean Photon Number at the Output Ports for Input States $a_1^\dagger|0\rangle = |1\rangle_{1a}$ and $a_2^\dagger|0\rangle = |1\rangle_{2a}$ in the Presence of an Object

Ports \ Measurements	Input State $a_1^\dagger\|0\rangle = \|1\rangle_{1a}$	Input State $a_2^\dagger\|0\rangle = \|1\rangle_{2a}$
Port #3 $(D_{M_1}) \backslash \langle N_3 \rangle$	$\tilde{R}\tilde{T}$	$\tilde{T}^2$
Port #1 $(D_1) \backslash \langle N_1 \rangle$	$\tilde{R}^3$	$\tilde{R}^2\tilde{T}$
Port #2 $(D_2) \backslash \langle N_2 \rangle$	$\tilde{R}^2\tilde{T}$	$\tilde{R}\tilde{T}^2$
Port #4 $(D_{M_2}) \backslash \langle N_4 \rangle$	$\tilde{T}^2$	$\tilde{R}\tilde{T}$

reflection ($\tilde{R}$) is equal to the transmission ($\tilde{T}$) and is thus referred to as "symmetric". In the second configuration we consider $\tilde{R} \neq \tilde{T}$ and it is thus referred to as "asymmetric".

In addition, since the number of photons at each of the ports depend on the physical parameters of the system, we can characterize the system and determine $(\tilde{R}, \tilde{T}, \cos^2(\frac{\varphi}{2}))$ by these measurements (see Supplement 1).

3.1. Symmetric

The "symmetric" detection configuration is achieved when

$$\tilde{R} = \tilde{T}, \quad \varphi = 0. \tag{10}$$

These conditions lead to a complete destructive interference at port #1 (#2) for the input state $|1\rangle_{1a}$ ($|1\rangle_{2a}$), which we refer to as a dark port.

This configuration is akin to the well-known case considered by Elitzur and Vaidman [3], for a lossless symmetric Mach–Zehnder.

The IFM detection probability P_{det}, namely, the probability to detect an object without absorption by the object is

$$P_{\text{det}} = \frac{\tau^3}{8}. \tag{11}$$

The IFM detection efficiency in this case is (see Supplement 1 for more detail)

$$\eta^{(\text{Symmetric})}(\tau) = \frac{\tau}{2 + \tau}. \tag{12}$$

For the lossless case $\tau \to 1$, we reproduce the known efficiency of $\eta^{(\text{Symmetric})}(\tau \to 1) \equiv \eta_{\text{max}} = \frac{1}{3}$, which is also equivalent to the dose reduction η^{dose}. It is worth noting that due to symmetry, the efficiency is independent of the input photon port number (#1 or #2). The probability of detecting an object by either IFM or absorption by the object is given by

$$P(\text{tot. det}) = \frac{\tau^2}{4}\left(\frac{\tau}{2} + C\right). \tag{13}$$

More details concerning the confidence C can be found in Supplement 1. Note that for $(\tau = 1 \Leftrightarrow C = 1)$ the total detection probability reaches its maximal value $P(\text{tot. det}) = \frac{3}{8}$. The dose reduction in this case (see Fig. 3) is possible for $\tau > 0.705$ and has the maximal value of $\eta_{\text{max}}^{\text{dose}} = \frac{1}{3}$ in the lossless case. The dose reduction in this case is considerable for in the low-loss regime; for 10%–15% loss, a dose reduction of $\eta^{\text{dose}} \sim 0.108$–0.15. This configuration allows good IFM efficiencies with significant dose reduction in the low-loss regime and is experimentally since it does not require fine-tuning a phase term.
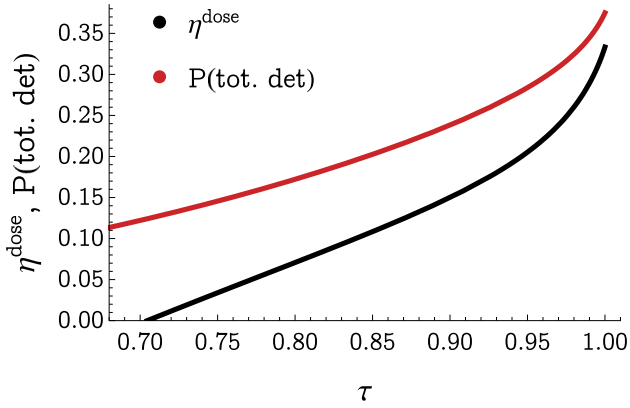
Fig. 3. Dose reduction parameter (η^{dose}) (solid black line) and total detection probability ($P(\text{tot. det})$) (solid red line) for the symmetric configuration as a function of the loss parameter τ.

3.2. Asymmetric

The "Asymmetric" detection configuration is achieved for $\varphi = \pi$, independently of the values of $(\tilde{R}, \tilde{T})$.

Following these conditions, port #2 (#1) is dark for the input state $|1\rangle_{1a}$ ($|1\rangle_{2a}$). In this configuration, the detection efficiency given by

$$\eta^{(\text{Asymmetric})}(\tilde{R}, \tilde{T}) = \begin{cases} \eta_1 = \dfrac{\tilde{R}}{1 + \tilde{R}}, & \text{for input } a_1^\dagger |0\rangle = |1\rangle_{1a}, \\ \eta_2 = \dfrac{\tilde{T}}{1 + \tilde{T}}, & \text{for input } a_2^\dagger |0\rangle = |1\rangle_{2a}, \end{cases}$$

(14)

depends on the input state, namely, whether the incident photon entered port #1 ($a_1^\dagger |0\rangle = |1\rangle_{1a}$) or port #2 ($a_2^\dagger |0\rangle = |1\rangle_{2a}$), and on the values of $(\tilde{R}, \tilde{T})$ (see Supplement 1 for more detail). The probability of detecting an object by either IFM or absorption by the object [see Fig. 4(b) and Fig. 5(b)], is given by

$$P(\text{tot. det}; \tilde{R}, \tilde{T}, C)$$
$$= \begin{cases} P_1(\text{tot. det}) = \tilde{R}\tilde{T}(\tilde{R} + C), & \text{for input } a_1^\dagger |0\rangle = |1\rangle_{1a}, \\ P_2(\text{tot. det}) = \tilde{R}^2(\tilde{T} + C), & \text{for input } a_2^\dagger |0\rangle = |1\rangle_{2a}. \end{cases}$$

(15)

More details concerning the confidence C can be found in Supplement 1. The total detection probability is maximal for $R = (\frac{1}{\sqrt{3}}, 1)$ for $(P_1(\text{tot. det}), P_2(\text{tot. det}))$, respectively, with maximal values of $(P_1^{\max}(\text{tot. det}) = \sqrt{\frac{4}{27}}, P_2^{\max}(\text{tot. det}) = 1)$ at $\tau = 1$. The dose reduction for the asymmetric configurations has relatively similar profile (see Fig. 4(a) and Fig. 5(a)) and for both a dose reduction is possible for $\tau > \frac{1}{2}$. The maximal dose reduction is $\eta_{\max}^{\text{dose}} = \frac{1}{2}$ in the lossless case. This configuration allows a substantial dose reduction in the low-loss regime. For (25%, 15%, 5%) loss, a dose reduction of $\eta^{\text{dose}} \sim (0.2, 0.259, 0.31)$ can be reached, respectively. The total detection probability profile $P_2(\text{tot. det})$ decreases rapidly for increasing values of T, which suggests that this configuration is sub-optimal for high values of η_2^{dose} as it require longer runtime compared with $\eta_1^{(\text{dose})}$. On the other hand, the first configuration can provide high dose reduction with reasonable probabilities and is

(a) Dose reduction parameter η_1^{dose}

(b) Total detection probability $P_1(\text{tot. det})$
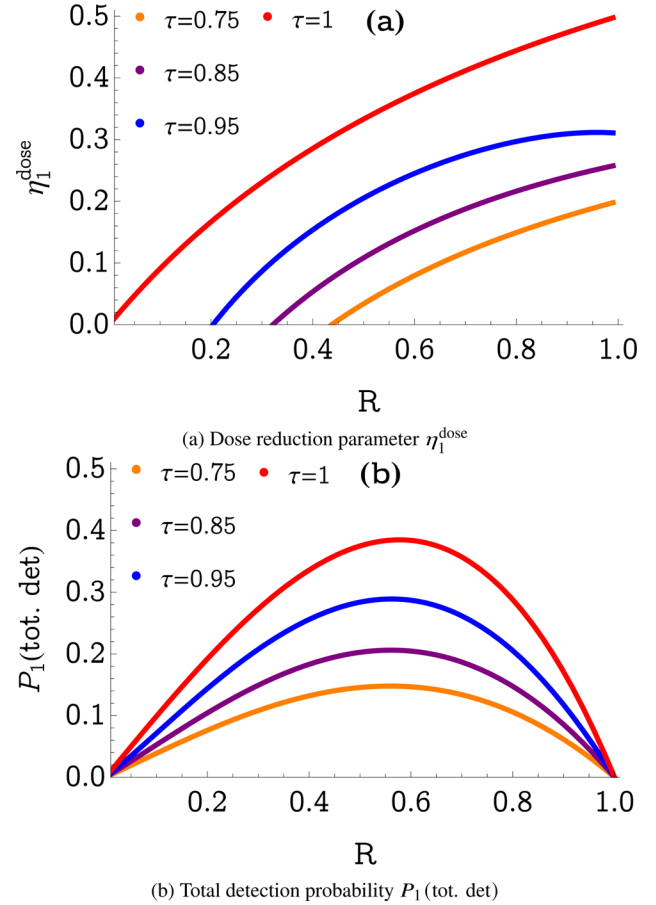
Fig. 4. (a) Dose reduction parameter (η_1^{dose}) and (b) the total detection probability [$P_1(\text{tot. det})$] for the asymmetric configuration, which corresponds to the input state $|1\rangle_{1a}$, plotted a function of the reflection coefficient R for various values of the loss parameter τ. The orange line is for 25% ($\tau = 0.75$) loss, the purple line is for 15% ($\tau = 0.85$), the blue line is for 5% loss ($\tau = 0.95$), and the red line is for the lossless case ($\tau = 1$).

therefore preferable, in particular if the experimental runtime is limited.

4. LOSSY BEAM SPLITTER MODELING BASED ON LAUE DIFFRACTION

The theoretical description shown in previous sections relied on the possible modeling of Laue diffraction as a transfer matrix between input and output field modes (see Fig. 6). To accommodate this general formalism for x ray optics, here we show such modeling. It is based on the quantized Takagi–Taupin equations [25] for the field operators $a_1(z)$ and $a_2(z)$ accompanied by Langevin operators to account for loss,

$$\frac{\partial a_1(z)}{\partial z} = -\left(\alpha + \frac{i\Delta k_z}{2}\right) a_1(z) + i\kappa a_2(z) + \sqrt{2\alpha} f_1(z),$$
$$\frac{\partial a_2(z)}{\partial z} = -\left(\alpha - \frac{i\Delta k_z}{2}\right) a_2(z) + i\kappa a_1(z) + \sqrt{2\alpha} f_2(z).$$

(16)

The coefficients α, κ, Δk_z are the absorption coefficient, coupling coefficient and phase mismatch along the optical axis,

(a) Dose reduction parameter η_2^{dose}

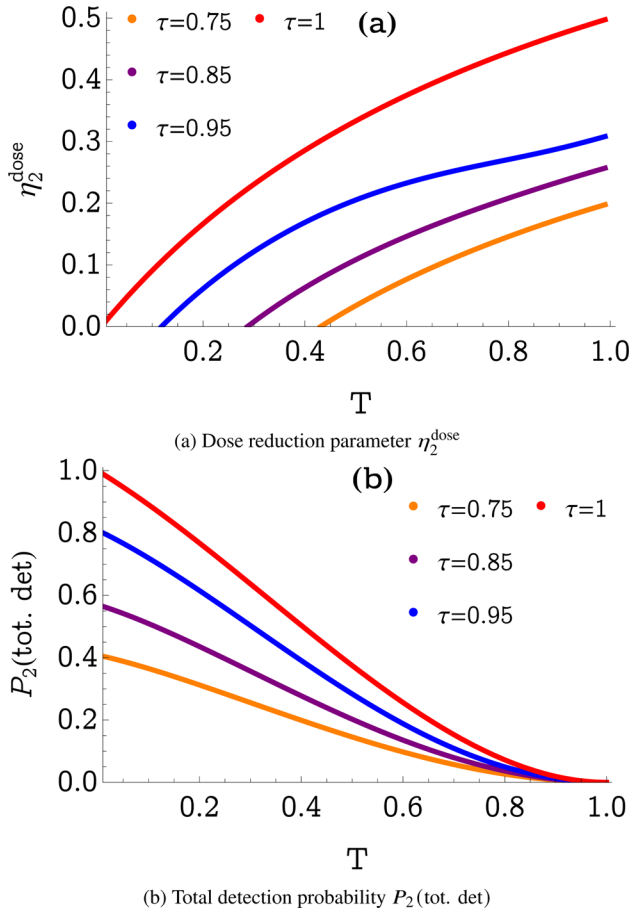(b) Total detection probability $P_2(\text{tot. det})$

Fig. 5. (a) Dose reduction parameter (η_2^{dose}) and (b) the total detection probability ($P_2(\text{tot. det})$) for the asymmetric configuration, which corresponds to the input state $|1\rangle_{2a}$, plotted as function of the transmission coefficient T for various values of the loss parameter τ. The orange line is for 25% ($\tau = 0.75$) loss, the purple line is for 15% ($\tau = 0.85$), the blue line is for 5% loss ($\tau = 0.95$), and the red line is for the lossless case ($\tau = 1$).
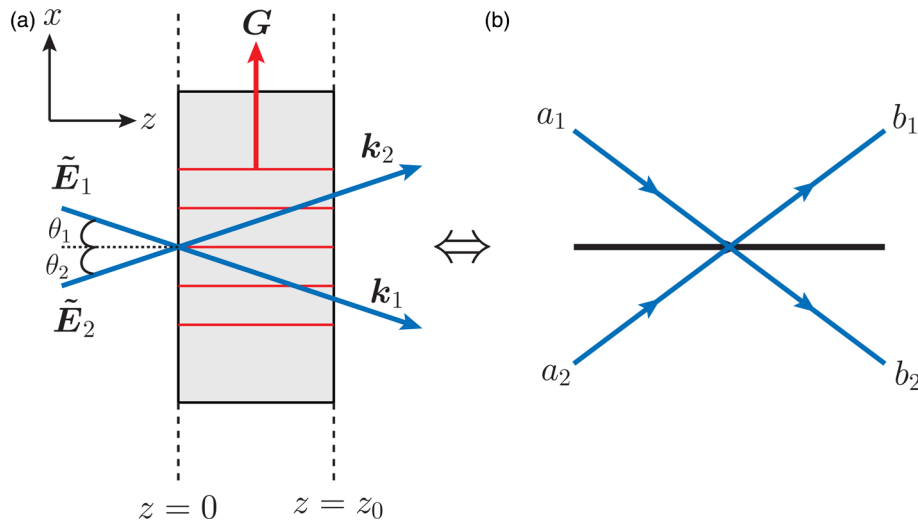
respectively. Their explicit form is given by

$$
\begin{aligned}
\alpha &= \tilde{\sigma}_0 \omega \gamma \rho_0, \\
\kappa &= \tilde{\sigma}_0 (\omega^2 - \omega_0^2) \rho_G, \\
\Delta k_z &= (\boldsymbol{k}_2 - \boldsymbol{k}_1 - \boldsymbol{G}) \cdot \hat{z}, \\
\tilde{\sigma}_0 &= -\frac{e\mu_0 c}{2m_e n \cos(\theta_b)} \frac{\omega}{\omega^2(1 + \gamma^2) - \omega_0^2}.
\end{aligned}
\tag{17}
$$

When the incident angles slightly deviate from Bragg's condition by a small parameter δ, such that $\theta_1 = \theta_b + \delta$, $\theta_2 = \theta_b - \delta$, the phase mismatch can be approximated $\Delta k_z \approx |\boldsymbol{G}|\delta$. The Lorentz model was used to describe the linear response for a periodic charge density

$$
\rho(\boldsymbol{x}) = \sum_G \rho_G e^{i\boldsymbol{G}\cdot\boldsymbol{x}},
\tag{18}
$$

such that ρ_G is the charge density Fourier component associated with reciprocal lattice vector $\boldsymbol{G}$ and ρ_0 is the mean electron charge density. The parameters $-e$, m_e, c, μ_0, ω_0, ω, γ, n, θ_b are the electron's charge, electron's mass, speed of light in vacuum, permeability of free space, resonance frequency of the Lorentz oscillator, field's frequency, damping coefficient, refraction index, and Bragg's angle, respectively. Following the solution of these equations, the relation between the input operators $\boldsymbol{a} = (a_1(0) \equiv a_1, \, a_2(0) \equiv a_2)$ and the output operators $(a_1(z_0), \, a_2(z_0))$ at z_0 is given by

$$
\begin{aligned}
a_1(z_0) &= e^{-\alpha z_0} \left(t^*(z_0)a_1 + ir(z_0)a_2\right) + \sqrt{1 - e^{-2\alpha z_0}} a_{n1}, \\
a_2(z_0) &= e^{-\alpha z_0} \left(ir(z_0)a_1 + t(z_0)a_2\right) + \sqrt{1 - e^{-2\alpha z_0}} a_{n2},
\end{aligned}
\tag{19}
$$

where

$$
\begin{aligned}
t(z) &= \text{sech}(\phi)\cos(\cosh(\phi)\kappa z + i\phi), \\
r(z) &= \text{sech}(\phi)\sin(\cosh(\phi)\kappa z),
\end{aligned}
\tag{20}
$$

and $\sinh(\phi) = -\frac{\Delta k_z}{2\kappa}$. The addition of the bosonic noise operators $\boldsymbol{a}_n = (a_{n1}, a_{n2})$ is required to ensure the commutation relations and their contribution is proportional to the loss. Rewriting this relation in terms of the output operators $\boldsymbol{b} = (b_1, b_2)$, as depicted
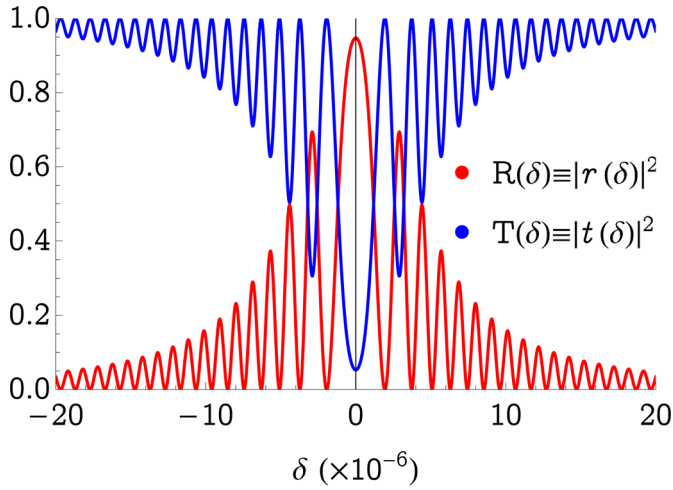

Fig. 6. (a) Fields ($\tilde{\boldsymbol{E}}_1$, $\tilde{\boldsymbol{E}}_2$) with wave vectors ($\boldsymbol{k}_1$, $\boldsymbol{k}_2$) at incident angles (θ_1, θ_2), respectively, undergo Laue diffraction with respect to the reciprocal lattice vector $\boldsymbol{G}$ by a crystal of width z_0. (b) Analogous representation of Laue diffraction as a beam splitter in which input operators (a_1, a_2) are transformed to output operators (b_1, b_2).

Fig. 7. Angular dependence of the lossless reflection (R) and transmission (T) coefficients (see Eq. (1)) on the mismatch angle δ in units of microradians for silicon crystal in the low-loss regime ($\tau \approx 0.994$).

in Fig. 6(b), yields

$$b(z) = e^{-\alpha z}\text{bs}(z)a + \sqrt{1 - e^{-2\alpha z}}a_n, \qquad (21)$$

where

$$\text{bs}(z) = \begin{pmatrix} ir(z) & t(z) \\ t^*(z) & ir(z) \end{pmatrix}. \qquad (22)$$

The transformation consists of two parts. The first term corresponds to a standard beam splitter transformation [bs(z)] which is attenuated by a factor of $e^{-\alpha z}$ due to absorption. The presence of loss gives rise to the second term which describes the additional noise. Controlling the transmission $T = |t|^2$ and reflection $R = |r|^2$ coefficients can be achieved by tuning the incident angle and thus modifying Δk_z. To illustrate this point, we show the angular dependence of (R, T) on the mismatch angle δ in Fig. 7, in the case of silicon with $z_0 = 200\,\mu$m, photon energy of $\hbar\omega = 30$ keV and diffraction plane of $(2, 2, 0)$.

In this example, $e^{-2\alpha z_0} \approx 0.994$ therefore, the loss is negligible and adequate control on R, T is possible by angular deviations of the order of approximately microradians. Furthermore, adequate tunability of R, T is feasible in the lossy domain as depicted in Fig. 8, which corresponds to the case of silicon with $z_0 = 500\,\mu$m, photon energy of $\hbar\omega = 18$ keV, diffraction plane of $(2, 2, 0)$, and absorption of $1 - e^{-2\alpha z_0} \sim 0.468$. In this case, the oscillation's frequency is larger which provides finer tunability of R, T. Despite the substantial loss ($\tau \approx 0.532$), our approach demonstrates notable resilience with achievable IFM efficiencies of approximately $\eta^{(\text{Symmetric})} \sim 0.21$ and $\eta^{(\text{Asymmetric})} \sim 0.34$. This example shows that high IFM efficiency can be obtained even when there is substantial loss.

5. DISCUSSION

We have shown that IFM (and in particular, x ray IFM with the LLL interferometer) is feasible even with significant loss. Our analysis highlights the quantitative robustness of IFM to loss, despite being a coherence-based phenomenon. The effect of loss inherently decreases the overall detection efficiency originating from both IFM events and absorption events, since both the IFM efficiency and the confidence level in detection via absorption,
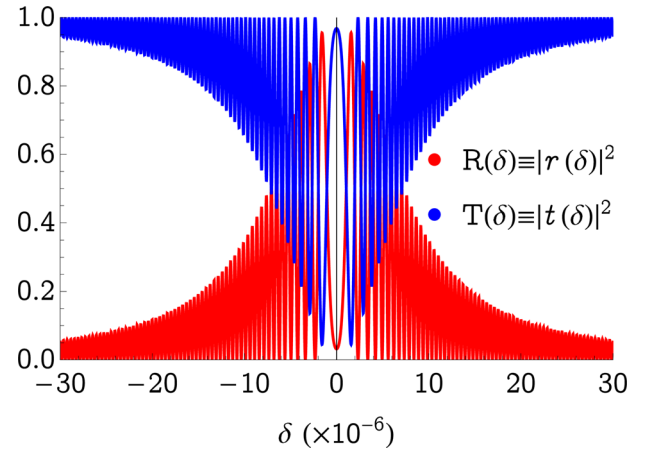

Fig. 8. Angular dependence of the lossless reflection (R) and transmission (T) coefficients (see Eq. (1)) on the mismatch angle δ in units of microradians for silicon crystal in the lossy regime ($\tau \approx 0.532$).

decrease with loss. Despite this limitation, we have shown that employing IFM as a detection scheme can lead to dose reduction with an impressive resilience to loss.

We have analyzed two IFM detection configurations with IFM efficiencies ranging from $\frac{1}{3}$ to $\frac{1}{2}$ and dose reduction of up to half compared with direct detection. The symmetric configuration is slightly simpler to implement, since it does not require a fine-tuning phase. In this configuration, dose reduction is achievable under loss of up to $\sim 30\%$ ($\tau > 0.705$), and at best can asymptotically reach $\eta^{\text{dose}} \rightarrow \frac{1}{3}$ (in the absence of loss). In the presence of low-loss ($10 - 15\%$), reasonable dose reduction can still be reached ($\eta^{\text{dose}} \sim 0.108 - 0.15$) and thus it is a promising experimental configuration, provided there is an adequate control on the reflection ($\tilde{R}$) and transmission ($\tilde{T}$) coefficients. The asymmetric configuration is preferable for a scenario in which a well-controlled phase can be introduced (without adding loss) to the setup. In addition, it can be important for cases in which there is limited control of the ratio between the reflection and transmission coefficients ($\tilde{R}, \tilde{T}$). In this configuration dose reduction is achievable under loss of up to 50% ($\tau > \frac{1}{2}$), and at best can reach asymptotically $\eta^{\text{dose}} \rightarrow \frac{1}{2}$ (in the absence of loss), if the ratio $\frac{\tilde{R}}{\tilde{T}}$ can be controlled. In the presence of low-loss (10%–15%), good dose reduction can be reached ($\eta^{\text{dose}} \sim 0.259$–$0.285$) and thus can be used to demonstrate efficient x ray IFM with significant dose reduction despite the presence of loss.

Furthermore, due to the symmetry of the LLL setup, the results presented here are independent of the way one models the beam splitters (provided they are identical). However, in order to properly design an LLL system in practice, it is instructive to have a model of a lossy beam splitter which is based on Laue diffraction. For this purpose, we constructed such a model and showed that adequate control of the ratio $\tilde{R}/\tilde{T}$ is possible while remaining in the low loss regime as well as in the lossy regime. Such tunability suggests that x ray IFM can be demonstrated with high efficiency in the presence of significant loss in the system.

In addition, we have presented a convenient method to experimentally characterize the properties of the interferometer. This method allow for the determination of the key parameters $\tilde{R}, \tilde{T}$, and $\cos^2(\frac{\varphi}{2})$, using only the measurements of the outgoing ports.

In conclusion, our study demonstrates the feasibility of x ray IFM using the LLL interferometer. A successful demonstration of IFM in the x ray regime has great potential for delving into more advanced schemes for high efficiency IFM, e.g., high efficiency interrogation and imaging based on the quantum Zeno effect, as well as x ray IFM for semi-transparent objects. These developments lend support to the advancement of low-dose x ray imaging techniques based on IFM.

Disclosures. The authors declare no conflicts of interest.

Data availability. All relevant data are available within the article and Supplement 1.

Supplemental document. See Supplement 1 for supporting content.

REFERENCES

1. M. Renninger, "Messungen ohne störung des meßobjekts," Z. Physik **158**, 417–421 (1960).
2. R. Dicke, "Interaction-free quantum measurements: A paradox?" Am. J. Phys. **49**, 925–930 (1981).
3. A. C. Elitzur and L. Vaidman, "Quantum mechanical interaction-free measurements," Found. Phys. **23**, 987–997 (1993).
4. L. Vaidman, "On the realization of interaction-free measurements," Quantum Opt. **6**, 119–124 (1994).
5. P. Kwiat, H. Weinfurter, T. Herzog, *et al.*, "Interaction-free measurement," Phys. Rev. Lett. **74**, 4763–4766 (1995).
6. P. G. Kwiat, "Experimental and theoretical progress in interaction-free measurements," Phys. Scr. **T76**, 115 (1998).
7. T. Tsegaye, E. Goobar, A. Karlsson, *et al.*, "Efficient interaction-free measurements in a high-finesse interferometer," Phys. Rev. A **57**, 3987–3990 (1998).
8. A. G. White, J. R. Mitchell, O. Nairz, *et al.*, ""Interaction-free" imaging," Phys. Rev. A **58**, 605–613 (1998).
9. Y. Zhang, A. Sit, F. Bouchard, *et al.*, "Interaction-free ghost-imaging of structured objects," Opt. Express **27**, 2212–2224 (2019).
10. A. M. Pălici, T.-A. Isdrailă, S. Ataman, *et al.*, "Interaction-free imaging of multipixel objects," Phys. Rev. A **105**, 013529 (2022).
11. L. Vaidman, *The Geometric Universe: Science, Geometry, and the Work of Roger Penrose* (Oxford University Press, 1998).
12. A. J. DeWeerd, "Interaction-free measurement," Am. J. Phys. **70**, 272–275 (2002).
13. J. Scuffham, M. Wilson, P. Seller, *et al.*, "A cdTe detector for hyper-spectral SPECT imaging," J. Instrum. **7**, P08027 (2012).
14. S. Send, A. Abboud, R. Hartmann, *et al.*, "Characterization of a pnCCD for applications with synchrotron radiation," Nucl. Instrum. Methods Phys. Res., Sect. A **711**, 132–142 (2013).
15. S. Sofer, E. Strizhevsky, A. Schori, *et al.*, "Quantum enhanced X-ray detection," Phys. Rev. X **9**, 031033 (2019).
16. E. Strizhevsky, D. Borodin, A. Schori, *et al.*, "Efficient interaction of heralded X-ray photons with a beam splitter," Phys. Rev. Lett. **127**, 013603 (2021).
17. F. Vagizov, V. Antonov, Y. Radeonychev, *et al.*, "Coherent control of the waveforms of recoilless γ-ray photons," Nature **508**, 80–83 (2014).
18. S. Huang, R. Duan, N. Pramanik, *et al.*, "Quantum recoil in free-electron interactions with atomic lattices," Nat. Photonics **17**, 224–230 (2023).
19. M. Hart, "Review lecture: Ten years of X-ray interferometry," Proc. R. Soc. Lond. A **346**, 1–22 (1975).
20. V. V. Lider, "X-ray crystal interferometers," Phys.-Usp. **57**, 1099–1117 (2014).
21. K.-D. Liss, R. Hock, M. Gomm, *et al.*, "Storage of X-ray photons in a crystal resonator," Nature **404**, 371–373 (2000).
22. S.-L. Chang, Y. P. Stetsko, M.-T. Tang, *et al.*, "X-ray resonance in crystal cavities: realization of Fabry-Perot resonator for hard x rays," Phys. Rev. Lett. **94**, 174801 (2005).
23. U. Bonse and M. Hart, "An X-ray interferometer," Appl. Phys. Lett. **6**, 155–156 (1965).
24. N. Namekata and S. Inoue, "High-efficiency interaction-free measurements using a stabilized Fabry–Pérot cavity," J. Phys. B: At. Mol. Opt. Phys. **39**, 3177–3183 (2006).
25. A. Authier, *Dynamical Theory of X-ray Diffraction*, Vol. 11 (Oxford University Press, 2004).